nature photonics

Article

https://doi.org/10.1038/s41566-023-01224-x

A chip-scale polarization-spatial-momentum quantum SWAP gate in silicon nanophotonics

Received: 10 March 2022

Accepted: 27 April 2023

Published online: 15 June 2023



Xiang Cheng ^{1,9} □, Kai-Chi Chang ^{1,9} □, Zhenda Xie^{1,2,3,9}, Murat Can Sarihan ¹, Yoo Seung Lee¹, Yongnan Li ¹, XinAn Xu², Abhinav Kumar Vinod¹, Serdar Kocaman ^{2,4}, Mingbin Yu^{5,6}, Patrick Guo-Qiang Lo^{5,7}, Dim-Lee Kwong⁵, Jeffrey H. Shapiro ⁸, Franco N. C. Wong⁸ & Chee Wei Wong ^{1,2} □

Recent progress in quantum computing and networking has enabled high-performance, large-scale quantum processors by connecting different quantum modules. Optical quantum systems show advantages in both computing and communications, and integrated quantum photonics further increases the level of scaling and complexity. Here we demonstrate an efficient SWAP gate that deterministically swaps a photon's polarization qubit with its spatial-momentum qubit on a nanofabricated two-level silicon photonics chip containing three cascaded gates. The on-chip SWAP gate is comprehensively characterized by tomographic measurements with high fidelity for both single-qubit and two-qubit operation. The coherence preservation of the SWAP gate process is verified by single-photon and two-photon quantum interference. The coherent reversible conversion of our SWAP gate facilitates examinations of a quantum interconnect between two chip-scale photonic subsystems with different degrees of freedom, now demonstrated by distributing four Bell states between the two chips. We also elucidate the source of decoherence in the SWAP operation in pursuit of near-unity fidelity. Our deterministic SWAP gate in the silicon platform provides a pathway towards integrated quantum information processing for interconnected modular systems.

Over the past few decades, quantum computing has undergone tremendous advances in the realization of quantum supremacy^{1,2} on a range of physical platforms^{3,4}. Optical quantum systems are a leading platform for achieving practical optically interconnected and distributed quantum computation⁵, which has been demonstrated to be scalable, in principle, with only linear optics⁶. Photons are potentially free

from decoherence and are easily manipulated in multiple degrees of freedom 7 , and effective interactions between photons are needed to construct an optical quantum computer realizable with optical quantum gates 8 . Universal quantum computing requires both single-qubit and two-qubit gate operations, the latter of which are usually probabilistic, leading to a large resource overhead that scales exponentially

¹Fang Lu Mesoscopic Optics and Quantum Electronics Laboratory, University of California, Los Angeles, CA, USA. ²Optical Nanostructures Laboratory, Columbia University, New York, NY, USA. ³National Laboratory of Solid State Microstructures and School of Electronic Science and Engineering, Nanjing University, Nanjing, China. ⁴Department of Electrical Engineering, Middle East Technical University, Ankara, Turkey. ⁵Institute of Microelectronics, Singapore, Singap

with the number of gates. Although cluster-state quantum computing has been proposed to drastically reduce resource overhead compared to the standard model^{9,10}, these cluster states cannot be prepared deterministically, and the probabilistic quantum-gates-associated resource overhead remains high¹¹. On the other hand, deterministic linear-optical quantum gates have been demonstrated utilizing several degrees of freedom (DoFs) of a single photon for multiple-qubit encoding¹². This scheme is equivalent to performing a unitary operation on a multidimensional qubit (or qudit) encoded into a single photon, and thus can be implemented with linear optics¹³. Such a deterministic two-qubit quantum gate will be beneficial for realizing a large-scale optical quantum computer due to its low resource overhead and high intrinsic success rate.

Optical quantum systems also provide a natural integration of quantum computation and quantum communication, which is promising regarding the ultimate goal of building a quantum internet 14,15. The quantum internet will enable quantum communications among remote quantum devices via quantum links, which will substantially scale up the number of qubits for distributed quantum computing¹⁶. Photonics channels can establish quantum links between distant stationary nodes with minimal loss and decoherence over long distances. Due to photons' well-defined Hilbert space in multiple DoFs, they are suitable for interconnecting with a range of photonic platforms and increasing communications rates with high-dimensional encoding^{17,18}. The recently developed integrated quantum photonics has opened another avenue for scaling up, and, taking advantage of wafer-scale fabrication processes, a state-of-the-art large-scale quantum device with more than 550 optical components has been demonstrated for multidimensional entanglement^{19,20}. These large-scale integrated photonics can increase the scale and complexity of quantum circuits, and a universal two-qubit unitary operation has been demonstrated that exploits high-dimensional entanglement in the path DoFs²¹.

Exploiting the photonics platform with a commercially available complementary metal-oxide-semiconductor (CMOS)-compatible process, we demonstrate an efficient silicon SWAP gate that deterministically swaps the polarization qubit with the spatial-momentum qubit from a single photon. The polarization DoF is easy to manipulate and measure using just waveplates and polarizing components, and the spatial-momentum DoF is naturally compatible with integrated photonics for path encoding and manipulation¹⁹. Our on-chip SWAP gate accesses these two DoFs by a concatenated scheme of three integrated controlled NOT gates: a specially designed momentum-controlled NOT (MC-NOT) gate sandwiched by two polarization-controlled NOT (PC-NOT) gates, with the two-stage MC-NOT gate nanofabricated in a self-aligned two-level silicon photonic process. We characterize the on-chip SWAP gate via state and process tomography with high fidelity for both single-qubit and two-qubit operation, with a single-qubit swapping process fidelity of up to $95.5 \pm 0.1\%$ and two-qubit swapping process fidelity of up to $94.9 \pm 2.0\%$. The preservation of quantum coherence in the on-chip SWAP operation of our silicon gate is verified by two-photon interference. The phase coherence of the on-chip SWAP operation is examined by single-photon self-interference with long-term stability. Furthermore, the reversible coherent conversion between the polarization and spatial-momentum qubits of our on-chip SWAP gate enables quantum interconnects. Enabled by the good single-chip performance, we demonstrate the quantum photonic interconnectivity by distributing four Bell states between two SWAP gates with a measured averaged Bell-state fidelity of $91.5 \pm 0.8\%$ in the polarization DoF after the second chip. Using a theoretical model, we also elucidate the source of possible errors for our silicon SWAP gate, including imperfect qubit rotation, spatial-mode contamination and unbalanced photon loss, and find good agreement with the measured truth-table fidelity of the on-chip SWAP operation. Our chip-scale deterministic SWAP gate provides unitary operation in the control of single and entangled photons, and its coherent reversible conversion enables a quantum photonic interconnect that will facilitate future distributed and cloud quantum computing^{22–24}.

Results

SWAP gate configuration and chip implementation

Figure 1a, left panel, presents a logic circuit schematic of the SWAP gate operation that swaps arbitrary values of qubits A and B without measuring or perturbing them. When qubits A and B are respectively encoded in the polarization and spatial-momentum modes of a single photon, a SWAP gate operation can be realized with the three-gate cascade shown in Fig. 1a, right panel²⁵. In probabilistic linear-optical quantum processing, most of the quantum logic operations are performed on two qubits, usually qubits of the same modality from two different photons. Here, a SWAP gate can coherently exchange states non-deterministically between qubits residing on different photons. In our single-photon two-qubit SWAP gate, qubit states are exchanged deterministically between the polarization and spatial-momentum DoFs of the same photon, which suggests that robust on-chip multi-qubit single-photon logic of higher order should be achievable²⁶⁻²⁹.

The polarization qubit (P) is based on the two polarization eigenstates $|H\rangle$ and $|V\rangle$, which correspond to the transverse electric (TE) and transverse magnetic (TM) polarizations of our quantum photonic chip. Our experiments use a type-II phase-matched spontaneous parametric downconversion (SPDC) waveguide source that produces $|V_SH_1\rangle$ biphotons in a single spatial mode, where the subscripts S and I denote the signal and idler qubits. The momentum qubit (M) is based on two spatial-momentum eigenstates $|T\rangle$ and $|B\rangle$, which correspond to the top and bottom channels of the quantum chip. Our experiments illuminate either the SWAP chip's top or bottom channels with polarization-rotated signal photons from the SPDC source, resulting in input state $|\Psi_{\rm T}\rangle_{\rm IN} = \left(|T_{\rm S}H_{\rm S}\rangle + {\rm e}^{i\varphi}\,|T_{\rm S}V_{\rm S}\rangle\right) \otimes |H_{\rm I}\rangle\,/\sqrt{2}$ for top-channel illumination and $|\Psi_{\rm B}\rangle_{\rm IN} = \left(|B_{\rm S}H_{\rm S}\rangle + {\rm e}^{i\varphi}\,|B_{\rm S}V_{\rm S}\rangle\right) \otimes |H_{\rm I}\rangle\,/\sqrt{2}$ for bottomchannel illumination, where $|H_1\rangle$ acts as a herald for the two qubits contained in its signal-photon companion. Defining $|0_{PS}\rangle = |H_S\rangle$, $|1_{PS}\rangle = |V_S\rangle$, $|0_{MS}\rangle = |T_S\rangle$ and $|1_{MS}\rangle = |B_S\rangle$ to be the logical-basis states, the input states become $\left|\varPsi_{T}\right\rangle _{IN}=\left(\left|0_{MS}0_{PS}\right\rangle +e^{i\phi}\left|0_{MS}1_{PS}\right\rangle \right)\bigotimes\left|H_{I}\right\rangle /\sqrt{2}$ and $|\Psi_B
angle_{lN}=\left(|1_{MS}0_{PS}
angle+e^{i\phi}\,|1_{MS}1_{PS}
angle
ight)igotimes|H_l
angle/\sqrt{2}$, which result in output states $|\Psi_{\rm T}\rangle_{\rm OUT} = \left(|1_{\rm MS}1_{\rm PS}\rangle + {\rm e}^{i\phi}\,|0_{\rm MS}1_{\rm PS}\rangle\right) \bigotimes |H_{\rm I}\rangle/\sqrt{2}$ and $|\Psi_{B}\rangle_{OUT} = \left(|1_{MS}0_{PS}\rangle + e^{i\phi} |0_{MS}0_{PS}\rangle\right) \bigotimes |H_{I}\rangle / \sqrt{2}, respectively. The signal$ photon's polarization and spatial-momentum gubits have been swapped and undergone a bit-flip.

The preceding SWAP operation is accomplished in our silicon photonics platform with three cascaded C-NOT gates designed so that the control and target qubits exchange roles in the middle C-NOT gate³⁰, as depicted in Fig. 1a, right panel. In our architecture, the PC-NOT gates are realized by a silicon-photonics polarized directional coupler, as shown in Fig. 1b. The silicon MC-NOT gate is realized by a specially designed two-layer polarization structure that, as shown in Fig. 1c, consists of two stages: (1) a polarization rotation stage, which tapers and rotates the qubit polarization by 90°, and (2) a polarization-maintaining mode conversion stage, which converts the qubit mode profile to match the output waveguide. The polarization rotation stage is shown in Fig. 1d. Because the polarization rotation and mode conversion are only implemented for the top channel, as shown in Fig. 1f, the two-layer polarization structure thus performs the MC-NOT operation. Detailed design-space maps and optimization of the MC-NOT and PC-NOT gates are described in Supplementary Section I.

Each of the PC-NOT and MC-NOT gates has a silicon-dioxide top cladding, with a rectangular silicon waveguide with a 460 nm \times 220 nm width-height cross-section, and with relatively small birefringence between the TE and TM modes for the polarization operations and diversity ^{31,32}. The optimized PC-NOT gate has a waveguide-to-waveguide gap of 400 nm with a designed 11.5- μ m coupling length, ensuring that the TE mode remains in its original waveguide while the TM mode

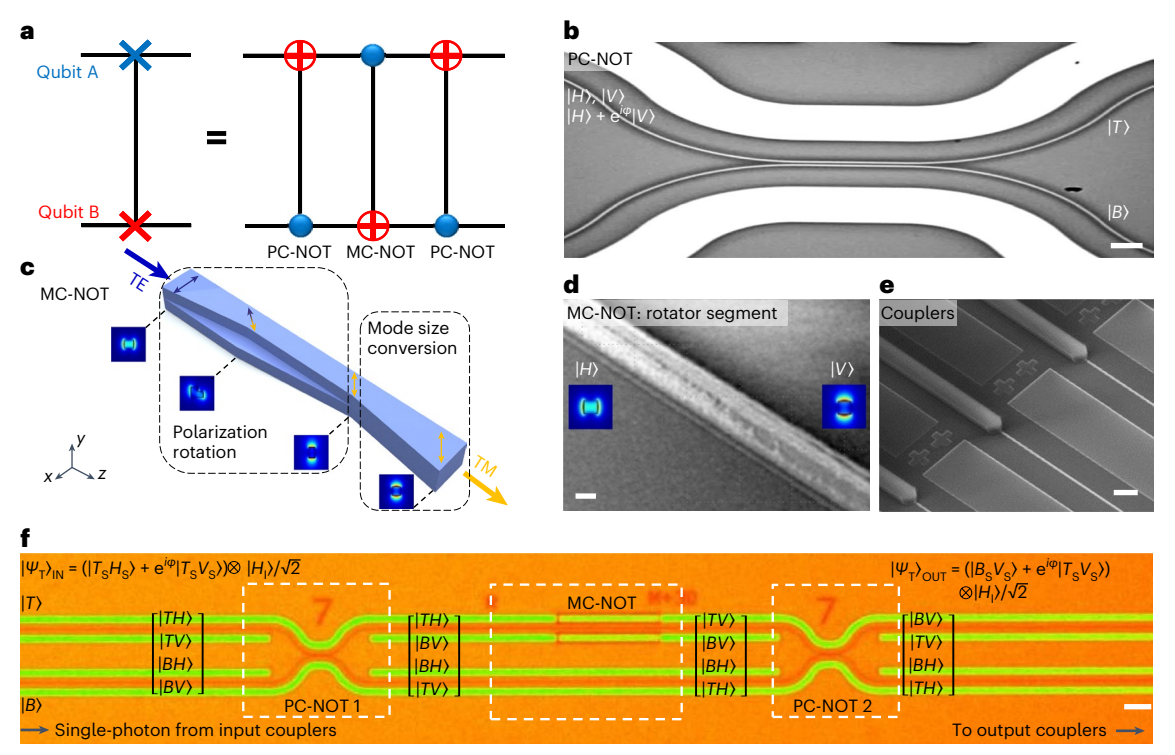


Fig. 1| A chip-scale polarization–spatial single-photon two-qubit SWAP gate. a, Illustrative logic circuit of the two-qubit SWAP gate. This can be realized for a single photon carrying qubit A in its polarization mode and qubit B in its spatial-momentum mode, by sequentially applying a PC-NOT gate, an MC-NOT gate and another PC-NOT gate, which are controlled by qubits A, B and A, respectively. **b**, Scanning electron microscopy (SEM) image of the chip-scale SWAP gate's first-stage PC-NOT gate realized by an optimized integrated-photonics polarized coupler. Scale bar, 2 μm. **c**, Schematic of an integrated two-level polarization rotator with polarization rotation and mode size conversion sections, enabling the second-stage MC-NOT gate for the SWAP

operation. **d**, SEM image of the MC-NOT gate's nanofabricated polarization rotation segment. Scale bar, 500 nm. **e**, SEM image of inverse taper couplers for improved free-space qubit-to-chip coupling. Scale bar, 20 μ m. **f**, Optical micrograph of the complete SWAP gate operation using the cascaded PC-NOT/MC-NOT/PC-NOT architecture. Scale bar, 10 μ m. An example of the input state ($|\Psi_T\rangle_{IN}$) for the top channel of the SWAP gate is shown, leading to the output state $|\Psi_T\rangle_{OUT}$, where the signal photon's polarization qubit is swapped to the spatial-momentum qubit. State vectors at each NOT gate segment represent the resulting states of each gate operation on four possible input states ($|TH\rangle$, $|TV\rangle$, $|BH\rangle$, $|BV\rangle$).

crosses over to the other waveguide, with an achieved average extinction ratio of ~18 dB for different input-output ports and polarization combinations (details are provided in Supplementary Section II). The optimized MC-NOT gate has two 110-nm step-height layers, and with tapered widths down to 150 nm and uniform 30-nm lateral offsets. This specially designed polarization rotator requires two-level fabrication with two-mask alignment. The misalignment of the two masks (or levels) creates scattering losses and reduces the polarization extinction ratio³³, limiting the performance of the resulting MC-NOT gate and ultimately the SWAP gate. To overcome misalignment, we have developed a self-aligned two-level nanofabrication approach to achieve the high extinction ratio required for the polarization rotator (as detailed in Supplementary Section II). Two mask layers serve as the single mask for the first 220-nm silicon reactive ion etch of the whole MC-NOT gate region, then the top layer is stripped via a resist developer, leaving the already-patterned hard mask. This hard mask is already self-aligned to the first etch and thus serves as the mask to define the 110-nm etch for the polarization rotator region in Fig. 1c. This self-alignment procedure eliminates the need for alignment between the two silicon etch steps, and only two-level alignment before the first etch is needed for a relatively flat surface for lithography patterning, resulting in a guaranteed 30-nm layer-to-layer offset without alignment error. Our designed MC-NOT gate achieved a high extinction ratio of ~20 dB for both TE and TM modes. The sidewall roughness is minimized for low waveguide loss, to ensure good SWAP gate performance. In addition, to ensure good coupling efficiency, adiabatic inverse tapers are designed for mode-index transformation at the input-output facets as shown in Fig. 1e, with less than 3-dB loss for each facet.

The silicon PC-NOT and MC-NOT gates were individually characterized using a swept tunable laser (Santec TSL-510). The transmission spectra of both gates were measured using a free-space coupling system, which selects the input and output channels for the gates. The input laser light's polarization was set by a polarizer and a half-wave plate (HWP) for $|H\rangle$ or $|V\rangle$, and the output light was measured by a polarizer. The on-chip PC-NOT and MC-NOT gates were found to have extinction ratios of more than 18 dB and 20 dB, respectively, over a 100-nm span range in the C band (transmission results are detailed in Supplementary Section II). Next, we characterized the on-chip SWAP gate performance using the same coupling system for the four basis states $|TH\rangle$, $|TV\rangle$, $|BH\rangle$ and $|BV\rangle$. Consistent performance was achieved from 1,550 nm to 1,560 nm with extinction ratios of more than 12 dB (transmission results are detailed in Supplementary Section III). The crosstalk suppression of the SWAP gate is mainly bounded by the finite extinction ratios of the PC-NOT and MC-NOT gates, as well as the polarization misalignment between the output waveguide mode and the projection polarizers. The total insertion loss of the SWAP gate chip was estimated to be ~6 dB; this could be further reduced by better engineering of the coupler structure³⁴.

Truth table of the on-chip SWAP gate

With sufficiently low crosstalk measured between the basis states, we next examined the heralded single-photon two-qubit SWAP operation

in the computational basis. Our single-photon two-qubit SWAP gate measurement set-up is shown schematically in Fig. 2a. Continuous-wave SPDC in a 1.5-cm ppKTP waveguide (AdvR) designed for type-II phase matching at ~1,556 nm produces orthogonally polarized signal-idler biphotons³⁵. The pump is a Fabry-Pérot laser diode stabilized with self-injection locking, through a double-pass first-order diffraction feedback with an external grating (details are provided in Supplementary Section IV)36. Tunable single-longitudinal mode lasing is achieved between 775.0 nm and 793.0 nm, enabling tunable SPDC with signal wavelengths from 1,552.5 to 1,559.6 nm, as shown in the inset of Fig. 2a. A long-pass filter blocks the residual pump photons after the SPDC, and an angle-mounted bandpass filter with an optical depth of 5 to 6 and a 95% passband transmission (Semrock NIRO1-1570/3) further suppresses pump photons. Here, the biphoton state $|V_sH_t\rangle$ is generated by SPDC. The signal and idler photons are then separated by the polarization beamsplitter (PBS). The signal photons are fed to the SWAP gate while the idler photons are directed to the superconducting nanowire single-photon detector (SNSPD; Photon Spot with ~85% detection efficiency) for heralding. A two-in two-out free-space coupling system accesses the top and bottom channels of the SWAP chip at both its input and output facets. For each input channel, half-wave (HWP), quarter-wave (QWP) and/or multi-order wave (MWP) plates control the input polarization state for each measurement set-up shown in Fig. 2a. The polarization state of the signal photon becomes $|H\rangle$ or $|V\rangle$ or the superposition state given earlier according to the waveplate combination. The input spatial-momentum state is controlled by switching the input fibre (blue dashed line) to the top or bottom channel of the SWAP gate, resulting in $|T\rangle$ or $|B\rangle$. For the truth-table measurements, the input states to our SWAP gate are in the four-dimensional Hilbert space spanned by $|TH\rangle$, $|TV\rangle$, $|BH\rangle$ and $|BV\rangle$, corresponding to $|00\rangle$, $|01\rangle$, $|10\rangle$ and $|11\rangle$ in the logical basis. Polarizers P_2 and P_3 are rotated for polarization projection at the output ports. Coincidence counting is then performed using SNSPDs at the P2 and P3 outputs with internal timing delays to match that of the heralding detection. By recording the coincidence rates for different polarization projections, we obtained the SWAP gate's truth table.

We first measured the logical operation of our PC-NOT gate by selecting an individual PC-NOT gate located on the same chip as our SWAP gate, with the same parameters as the SWAP gate's PC-NOTs. The characterization was performed using the measurement scheme shown in Fig. 2a (I). Figure 2b shows the resulting measured truth table obtained for the four input states $|00\rangle$, $|01\rangle$, $|10\rangle$ and $|11\rangle$ in the computational basis. The solid bars depict the experimentally measured truth table $M_{\rm exp}$ and the transparent bars illustrate the ideal truth table $M_{\rm ideal}$. The fidelity of the measured PC-NOT truth table with respect to the ideal one is calculated by $F=(1/4)\,{\rm Tr}\left(\frac{M_{\rm exp}M_{\rm ideal}}{M_{\rm ideal}M_{\rm ideal}}^{\rm T}\right)$. In our PC-NOT gate,

we achieved an average fidelity of 97.8 \pm 0.3% across the four basis states. We note that the residual deviation from unit fidelity is bounded by the PC-NOT's finite polarization extinction ratio (detailed in Supplementary Sections I and II) and the -0.9 dB coupling difference between the $|H\rangle$ and $|V\rangle$ states. Similarly, to characterize our MC-NOT gate, we measured an individual polarization rotator located on the same chip, with the same parameters as the SWAP gate's MC-NOT. The test polarization rotator only has one spatial mode (Fig. 2c, top inset), so the truth table was only measured for two input polarization states: $|0\rangle$ and $|1\rangle$. The fidelity of the measured truth table in Fig. 2c with respect to the ideal one was 98.0 \pm 0.2%. We can infer the good performance of our on-chip MC-NOT gate, which is effectively a two-channel scheme of the polarization rotator and a silicon waveguide.

Having demonstrated the good performance of each individual gate in the logical basis, we next measured the truth table of our on-chip SWAP gate. The truth table was measured by four measurements, each for four input states. We recorded a total of ~100,000 coincidence counts in $160\,\mathrm{s}$ for the truth-table measurements, yielding a

truth-table fidelity of 97.4 \pm 0.2% at 1,557 nm, supporting the excellent performance in the logical basis. Truth-table measurements were also performed at 1,556 nm and 1,558 nm with similar fidelity (details are provided in Supplementary Section V), consistent with the broadband performance of the classical characterization. We attribute the deviations from unity in the truth-table fidelity mainly to the imperfect extinction ratio of the PC-NOT and MC-NOT gates and the MC-NOT gate's unbalanced photon loss.

$\label{eq:Quantum state} \textbf{Quantum state and process tomographies for the on-chip SWAP gate}$

Although the truth table measures the two-qubit SWAP operation in the logical basis, quantum process tomography is required to completely characterize the Hilbert space of the SWAP gate operation^{30,37}. First, we used bulk optics to prepare the signal photons in an input set of six polarization states $\rho_{\text{pol}}(|H\rangle, |V\rangle, |D\rangle, |A\rangle, |R\rangle, |L\rangle$, as detailed in Supplementary Section VI), which were applied individually to the spatial input channels to the SWAP gate. Measuring the corresponding output spatial-momentum states ρ_{sm} provided the quantum state tomography for these polarization inputs. The six input polarizations are shown in the centre of Fig. 3a as Bloch vectors, and the reconstructed density matrices for each polarization state are provided in Supplementary Section VI. Two customized Mach-Zehnder interferometers (MZIs) with an extinction ratio of over 20 dB and two tunable delay lines were used to adjust the input spatial-momentum modes for the on-chip SWAP gate and project the output qubit on a set of six spatial-momentum states after the SWAP operation, respectively, with the measurement set-up shown in Fig. 2a (experiment II). The output spatial-momentum states were then analysed to perform quantum state tomography, with coincidence counts collected from the two $output \, ports \, of the \, MZI. \, Bloch-sphere \, representations \, of the \, measured$ $output\,spatial\text{-}momentum\,states\,are\,shown\,in\,Fig.\,3a.\,The\,state\,fidel-$

ity is defined as $F=(\mathrm{Tr}(\sqrt{\sqrt{\rho_{\mathrm{pol}}\rho_{\mathrm{sm}}\sqrt{\rho_{\mathrm{pol}}}}))$, which describes the overlap between the input polarization states and the measured output spatial-momentum states. For different spatial inputs, we achieved an averaged fidelity $\bar{F}_{\mathrm{QST},T}$ of 97.2 \pm 0.3% for the $|T\rangle$ input, $\bar{F}_{\mathrm{QST},B}$ of 97.4 \pm 0.3% for the $|B\rangle$ input, $\bar{F}_{\mathrm{QST},+}$ of 97.1 \pm 0.2% for the $|+\rangle$ input and $\bar{F}_{\mathrm{QST},+i}$ of 97.0 \pm 0.1% for the $|+i\rangle$ input. Reconstructed density matrix results for each spatial input are given in Supplementary Section VI. These high-fidelity output spatial-momentum states, with an average fidelity of 97.3 \pm 0.3%, confirm the successful single-qubit conversion from polarization qubit to spatial-momentum qubit.

Figure 3b shows the resulting process matrices of our SWAP gate for different spatial inputs. This SWAP gate operation process can be represented by a reconstructed process matrix χ , defined as $\rho_{\rm sm} = \sum_{mn} \chi E_m \rho_{\rm pol} E_n^{\dagger}$, where $E_{m(n)}$ are the identity I and Pauli matrices X, Y and Z, respectively. Thus, the SWAP gate's process matrix can be $experimentally \, reconstructed \, by \, quantum \, state \, tomography \, (Fig. \, {\color{blue}3a}).$ The process fidelity is defined as $F_{\chi} = \frac{\text{Tr}(\chi x_i)}{\text{Tr}(\chi)\text{Tr}(\chi_i)}$, where χ_i is the theoretically ideal process matrix. The X, Y and Z components of matrix χ represent the probability of bit-flip or phase-flip errors in the SWAP operation. We also evaluate the purity of the SWAP process matrix χ , defined as $P_{\chi} = \frac{\text{Tr}(\chi^2)}{\text{Tr}^2(\chi)}$, which is unity for an ideal process. Our SWAP gate is found to achieve a quantum process fidelity $\bar{F}_{\chi,T}$ of 95.5 \pm 0.2% with a process purity of 91.6 \pm 0.2% for the $|T\rangle$ spatial-momentum mode input, $\bar{F}_{\chi,B}$ of 95.3 ± 0.2% with a process purity of 91.6 ± 0.6% for the $|B\rangle$ input, $\vec{F}_{\chi,+}$ of 95.6 ± 0.2% with a process purity of 91.5 ± 0.2% for the $|+\rangle$ input, and $\bar{F}_{\chi,+i}$ of 95.4 ± 0.1% with a process purity of 91.2 ± 0.3% for the $|+i\rangle$ input. The average process fidelity for all spatial-momentum input modes is $95.5 \pm 0.1\%$, verifying the single-qubit SWAP operation of our silicon gate from polarization to spatial-momentum DoF.

For complete characterization of the two-qubit SWAP operation of our gate, we performed the full quantum process tomography.

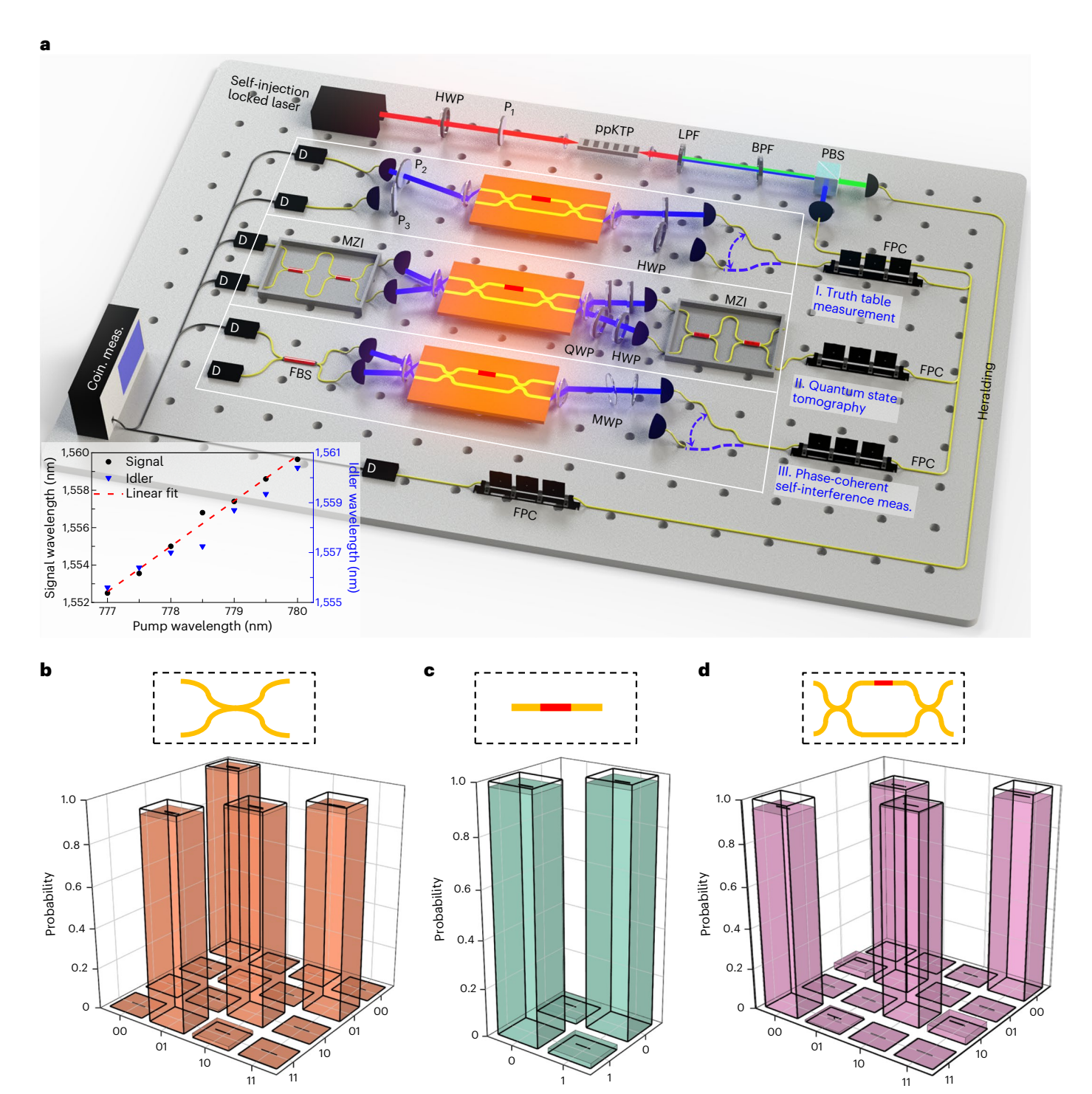


Fig. 2 | Experimental configuration for characterization of the single-photon two-qubit SWAP gate and truth-table measurements. a, Schematic of the heralded single-photon measurements generated via SPDC, with three modular experiments: (I) truth-table characterization, (II) quantum state tomography and (III) phase-coherence self-interference measurements. Input polarization qubits are controlled by a half-wave plate (HWP) and then fed to the gate through free-space coupling. Output spatial-momentum qubits are examined by a polarization analyser for truth-table measurements, by Bloch state measurements for the quantum state tomography, and interfered in a 50:50 beamsplitter for phase preservation checks on the SWAP operation. Successful SWAP operation is heralded by coincidence counting between the signal and

heralding channel. P_{ν} linear polarizer; LPF, long-pass filter; BPF, bandpass filter; PBS, polarization beamsplitter; FPC, fibre polarization controller; MWP, multiorder waveplate; QWP, quarter-wave plate; MZI, Mach–Zehnder interferometer; FBS, 50:50 fibre beamsplitter; D, superconducting nanowire single-photon detector. Bottom left inset: signal and idler photon wavelengths as a function of the pump wavelength. The red dashed line is a linear fit on the signal-photon wavelength. $\mathbf{b}-\mathbf{d}$, Measured (solid bars) and ideal (transparent bars) truth table for the PC-NOT gate (\mathbf{b}), MC-NOT gate (\mathbf{c}) and SWAP gate (\mathbf{d}) in the computational basis. A total of about 100,000 coincidence counts are recorded in 160 s for each measurement, yielding an average fidelity of 97.8 \pm 0.3%, 98.0 \pm 0.2% and 97.4 \pm 0.2%, respectively.

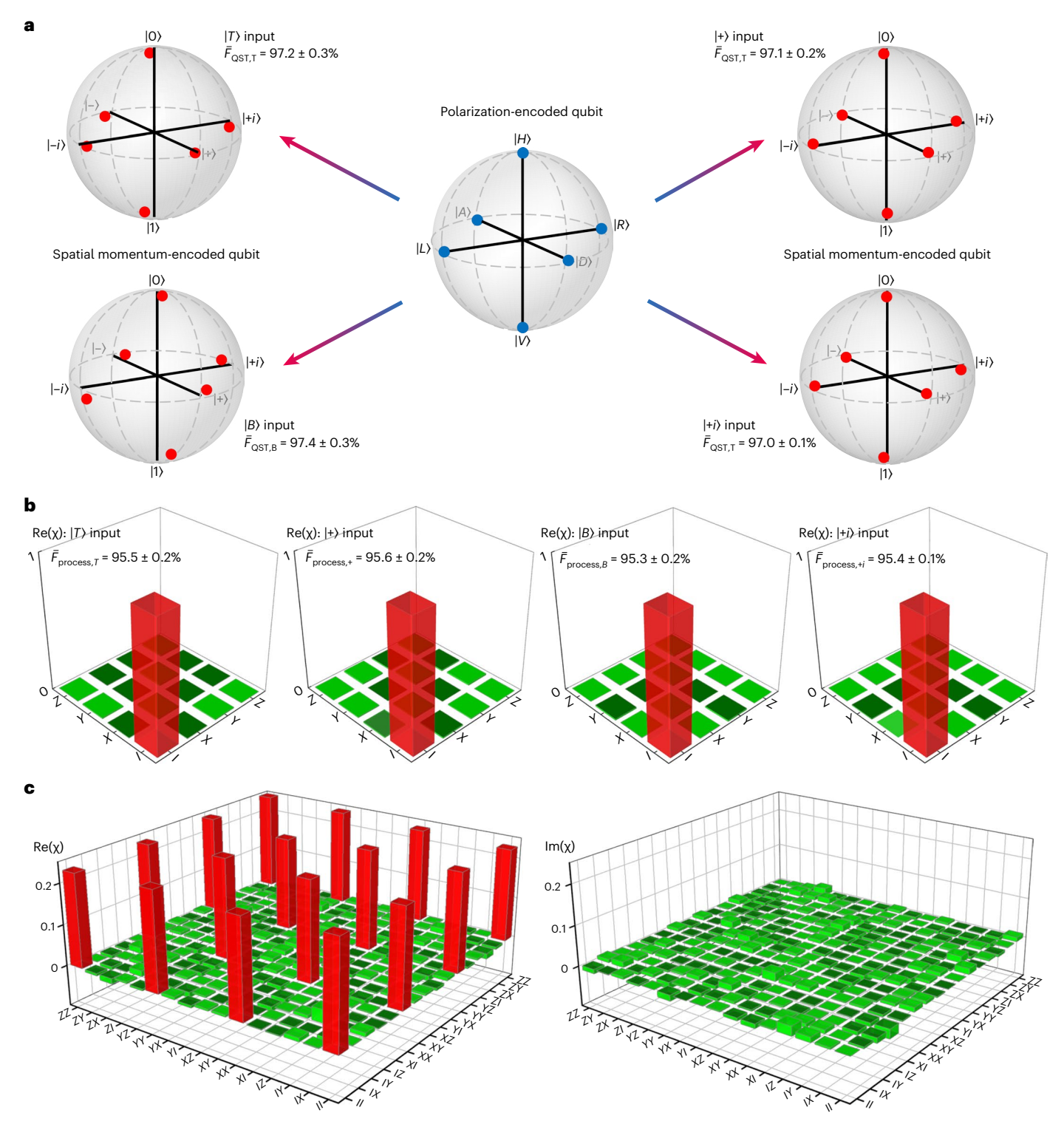


Fig. 3 | Quantum state and process tomographies for one-qubit and two-qubit SWAP operation. a, Output spatial-momentum-encoded states $|0\rangle, |1\rangle, |+\rangle, |-\rangle, |+i\rangle$ and $|-i\rangle$ measured by an MZI, represented by red dots on the Bloch sphere for input polarization qubits prepared in $|T\rangle, |B\rangle, |+\rangle$ and $|+i\rangle$ spatial-momentum modes. The indicated fidelities represent averages over the six measured states. Middle: Bloch-sphere representation of six polarization-encoded input states $|H\rangle, |V\rangle, |D\rangle, |A\rangle, |R\rangle$ and $|L\rangle$, prepared by bulk optics (blue dots). **b**, Real parts of the reconstructed single-qubit process matrix χ of the SWAP gate for $|T\rangle, |B\rangle, |+\rangle$ and $|+i\rangle$ spatial-momentum mode inputs, with an average process fidelity

of 95.5 \pm 0.1% and process purity of 91.5 \pm 0.2%. All imaginary elements of the process matrix are smaller than 0.05. **c**, Reconstructed process matrix χ of the single-photon two-qubit SWAP gate. Additional to Fig. 2a (II), HWPs, QWPs and polarizers are inserted before the MZI at the chip output for polarization qubit analysis. Quantum state tomography (QST) results of the 16 input two-qubit states are presented in Supplementary Section VI, with an averaged state fidelity of 96.1 \pm 0.8%. The two-qubit SWAP process fidelity is measured to be 94.9 \pm 2.0% with a process purity of 93.3 \pm 1.0%.

Additional to the process tomography measurement for single-qubit operation shown in Fig. 2a (II), waveplates and polarizers are inserted before the MZI at the output of the chip for the polarization qubit analysis. First, we prepared 16 separable, linearly independent states $\rho_{\rm sm,\,pol} = |i_{\rm sm}j_{\rm pol}\rangle$ as input two-qubit states, where $i_{\rm sm} = 0,\,1,\,+,\,+i$ and $j_{pol} = H$, V, D, R. The output states are projected in the same 16-state basis { $|i_{sm}j_{pol}\rangle$ }. The density matrix of the output states was reconstructed via quantum state tomography, with the results shown in Supplementary Section VI. An averaged state fidelity of $96.1 \pm 0.8\%$ is achieved for the 16 input states. The process matrix y was then reconstructed in a similar manner as for the single-qubit tomography using a block matrix of the measured density matrices (Fig. 3c; details are provided in the Methods)³⁸. We achieved a process fidelity of $94.9 \pm 2.0\%$ with a process purity of $93.3 \pm 1.0\%$, which demonstrates the on-chip two-qubit SWAP operation of our gate. In addition, we note the sources of process fidelity non-ideality come from the bulk-optics imperfections in generating the input polarizations, the differential propagation loss and coupling efficiency mismatch between the $|H\rangle$ and $|V\rangle$ states, and the residual misalignment of the spatial mode projection in the MZI.

Quantum coherence of the on-chip SWAP operation

An ideal SWAP operation is a coherent phase-preserving process. For a polarization input state of the form $|H\rangle + e^{i\varphi}|V\rangle$, the output state can be written as $|T\rangle + e^{i(\varphi+\delta)}|B\rangle$, where the phase difference φ between the orthogonal polarizations is transferred to the spatial modes and a constant phase δ accounts for the path-length difference between the $|T\rangle$ and $|B\rangle$ spatial-momentum modes at the output. The $|T\rangle$ and $|B\rangle$ SWAP outputs of the signal photon are combined with a 50:50 fibre beamsplitter (FBS), as shown in Fig. 2a (III), the outputs of which are detected in coincidence with the heralding idler photon to yield a self-interference measurement of the signal photon as a function of φ . An adjustable path delay ΔT (not illustrated in the schematic) is included in the bottom channel of the SWAP output for balancing the lengths of the two interferometer arms.

In our measurements we start with a 45° linearly polarized qubit $|D\rangle$, and the phase shift φ is introduced via a tuned pair of MWPs (illustrated in Fig. 2a (III)) with their optical axes aligned to the $|V\rangle$ polarization. They are mounted on two motorized rotation stages for simultaneous counter-rotation along their optical axes. A tunable phase delay φ is imposed between $|H\rangle$ and $|V\rangle$ at the input by applying a rotation θ to one waveplate, while the transverse displacement of the beam is cancelled with the counter-rotation with the same angle magnitude for the other waveplate. The SWAP gate chip and the interference paths are carefully isolated from environmental noise for the phase-sensitive measurements. By sweeping the relative phase φ between the $|H\rangle$ and $|V\rangle$ polarizations of the input state of the signal photon, we can probe the phase coherence of our SWAP gate operation by self-interference between the $|T\rangle$ and $|B\rangle$ output spatial-momentum states.

Figure 4a shows the self-interference fringes of the two spatial-momentum modes of the signal photon after the SWAP operation at different wavelengths. For the $|T\rangle$ spatial-momentum input state, a raw fringe visibility of $98.7 \pm 0.2\%$ is obtained (99.4% after background subtraction) at 1,556 nm. This interference can also be observed when the polarization qubit is input through the bottom channel, with a raw visibility of $98.0 \pm 0.2\%$ (98.5% after background subtraction). The phase coherent polarization-to-spatial-momentum SWAP operation was also verified at 1,557 nm and 1,558 nm with high-visibility fringes, as shown in Fig. 4a, obtaining a wavelength-averaged single-photon self-interference visibility of $98.7 \pm 0.4\%$. These observed high-visibility fringes demonstrate successful phase-coherence transfer from the input's polarization qubit to the output's spatial-momentum qubit. Moreover, we note that the phase interference is long-term robust and can maintain high visibility up to $96.6 \pm 0.3\%$ over 24 h in free-running

operation without feedback stabilization (details are provided in Supplementary Section VII), verifying phase-stable implementation of the on-chip single-photon two-qubit SWAP gate.

The coherence-preserved SWAP operation for two photons was further verified by off-chip Hong-Ou-Mandel (HOM) interference^{39,40}. which measures the indistinguishability of the two photons over all DoFs. Implementing the experimental set-up in Fig. 2a (I), both signal and idler photons are fed to the on-chip SWAP gate via the two-intwo-out coupling system, using HWPs to control the input polarization. At the output end, instead of the polarizers, the two output channels are connected to a HOM interferometer consisting of a 50:50 FBS and a delay line. A fibre polarization controller on one arm of the HOM interferometer ensures that the polarization of the two output photons will be the same at the FBS. By tuning the delay line, we can sweep the arrival time difference between the two output photons at the FBS and obtain the HOM interference dip. Figure 4b shows the measured HOM interference between the two output photons for different input polarization combinations. For the $|T_S V_S\rangle \bigotimes |B_1 H_1\rangle$ input, a HOM visibility of 96.9 (92.4) \pm 1.4% is obtained after (before) background subtraction. For the $|T_SH_S\rangle \otimes |B_IV_I\rangle$ input, a HOM visibility of 96.0 (91.0) \pm 1.9% is achieved after (before) background subtraction. The slightly lower visibility for the $|T_SH_S\rangle \otimes |B_1V_1\rangle$ input is because both signal and idler photons propagate through the polarization rotator on the upper arm of the SWAP gate, which introduces extra loss compared to the case for the $|T_S V_S\rangle \bigotimes |B_1 H_1\rangle$ input. The HOM dip width indicates the two-photon coherence time, which is measured to be 3.17 ± 0.02 ps for the $|T_SV_S\rangle \bigotimes |B_1H_1\rangle$ input and 3.11 ± 0.03 ps for the $|T_SH_S\rangle \bigotimes |B_1V_1\rangle$ input. The indistinguishability of the SPDC photon pairs was also examined using the same HOM interferometer (as detailed in Supplementary Section VIII), finding a HOM visibility of 97.9 (93.4) ± 1.0% after (before) background subtraction and a two-photon coherence time of 3.15 ± 0.02 ps. The small deviation of the HOM interference visibility and two-photon coherence time after the SWAP operation compared to the SPDC source unambiguously proves the preservation of the quantum coherence in the on-chip SWAP gate process. The observed HOM interference dip also verifies the indistinguishability between the two output spatial modes of the on-chip SWAP gate, which is crucial for path-mode entanglement generation on chip, enabled by quantum interference^{41,42}.

Quantum state distribution between dual SWAP gate chips

With coherence-preserved SWAP gate operation verified with high fidelity on our silicon chip, we next demonstrate an efficient quantum photonic interconnect between different DoFs utilizing the reversible conversion of our on-chip SWAP process. The experimental scheme of the chip-to-chip interconnect is illustrated in Fig. 4c. The input two-qubit maximally entangled state φ is prepared in the polarization basis. Polarization Bell state $|\Psi^+\rangle = (|HV\rangle + |VH\rangle)/\sqrt{2}$ is first generated by temporally overlapping the SPDC biphotons at a beamsplitter with orthogonal polarization (as detailed in the Methods)³⁶. The signal and idler photons are then fed to the $|T\rangle$ and $|B\rangle$ channels of the first SWAP gate chip, respectively. The input state can thus be written as $\varphi = (|H_S V_I\rangle + |V_S H_I\rangle) \bigotimes |T_S B_I\rangle / \sqrt{2}$. The first SWAP gate then deterministically swaps the entanglement from polarization to spatial-momentum, yielding $\varphi_{sm} = (|B_S T_I\rangle + |T_S B_I\rangle) \bigotimes |V_S H_I\rangle / \sqrt{2}$. The output spatial-momentum entangled state is transmitted to the second SWAP gate chip via a single-mode fibre link, where the polarization rotation during transmission is compensated by the QWPs and HWPs at the input of the second chip. The second SWAP gate has the same structural parameters as the first SWAP gate, and is characterized with a truth table $\bar{F}_{\rm gate,\,truth}$ of 97.2 \pm 0.3% (details are provided in Supplementary Section IX). The spatial-momentum entangled state is then reversibly converted to polarization entangled state φ by the second SWAP gate, and measured by polarization analysers consisting of a QWP, HWP and polarizer to perform quantum state tomography.

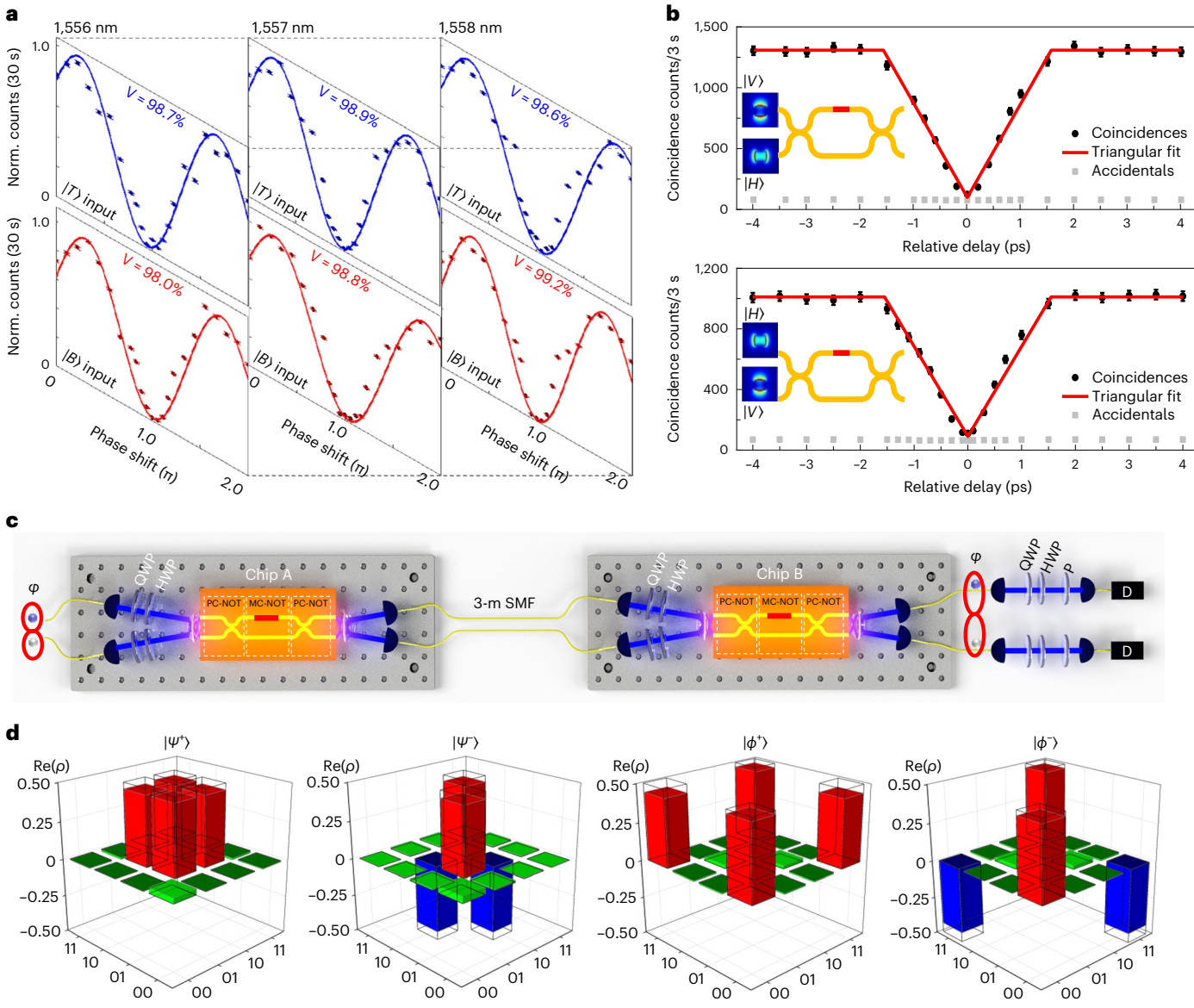


Fig. 4 | Coherence preservation of the SWAP gate and quantum state **distribution between dual SWAP gate chips. a**, A polarization qubit $|H\rangle + e^{i\varphi}|V\rangle$ is sent to the SWAP gate to probe the phase coherence of the single-photon two-qubit SWAP operation. Interference fringes are obtained by tuning the phase shift φ with a pair of MWPs (illustrated in Fig. 2a (III)), while collecting coincidence counts between signal and idler photons (accumulated for 30 s). Measured at 1,556 nm, 1,557 nm and 1,558 nm, the phase interference has fringe visibilities of $98.7 (99.4) \pm 0.2\%$, $98.9 (99.3) \pm 0.2\%$ and $98.6 (98.9) \pm 0.2\%$, respectively, for the $|T\rangle$ input state before (after) background subtraction. For the $|B\rangle$ input state, the fringe visibilities are 98.0 98.5) \pm 0.2%, 98.8 (99.0) \pm 0.2% and 99.2 (99.4) \pm 0.1%, respectively, before (after) background subtraction. b, Hong-Ou-Mandel interference between two photons after the SWAP operation for different input polarization combinations. A visibility of 96.9 (92.4) ± 1.4% is achieved for the $|T_SV_S\rangle \bigotimes |B_lH_l\rangle$ input and 96.0 (91.0) \pm 1.9% for the $|T_SH_S\rangle \bigotimes |B_lV_l\rangle$ input after (before) background subtraction, which proves the preservation of quantum coherence after the on-chip SWAP operation. Data are presented as mean

values \pm s.d. with n = 3. Error bars are calculated from three sets of measurements assuming Poissonian statistics. **c**, Experimental scheme for the quantum state distribution between two silicon SWAP gate chips. Polarization Bell states are prepared and fed into the first on-chip SWAP gate; then the swapped spatial-momentum states are transmitted through 3 m of single-mode fibre (SMF) and coupled to the second on-chip SWAP gate (the truth-table measurement is provided in Supplementary Section IX), which converts the spatial-momentum states back to the polarization states. Polarization analysers, consisting of a QWP, HWP and polarizer, measure the polarization entangled states after the second on-chip SWAP gate for tomographic characterization. **d**, Real parts of the reconstructed density matrices of the polarization Bell states $|\Psi^r\rangle$, $|\Psi^r\rangle$, $|\Psi^r\rangle$, and $|\Phi^r\rangle$, with an averaged Bell-state fidelity of 91.5 \pm 0.8% after the chip-to-chip distribution, verifying the coherent reversible conversion of the SWAP operation between two silicon chips. The imaginary parts of the density matrices are negligible.

By adjusting the HWPs and QWPs at the input of the first SWAP gate, the other three Bell states $|\Psi^-\rangle$, $|\Phi^+\rangle$ and $|\Phi^-\rangle$ can be produced for chip-to-chip distribution⁴³.

Figure 4d shows the experimentally reconstructed density matrices for four polarization Bell states. The state fidelity is calculated by $\frac{2}{2}$

 $F_{\text{Bell}} = (\text{Tr}(\sqrt{\sqrt{\rho_{\text{Ideal}}\rho_{\text{Bell}}}\sqrt{\rho_{\text{Ideal}}}})^2$, which describes the overlap between

the ideal Bell states and the measured states. The fidelities of the reconstructed density matrices compared to the corresponding Bell states are $F_{|\Psi^{+}\rangle}=92.5\pm0.3\%$, $F_{|\Psi^{-}\rangle}=90.4\pm0.5\%$, $F_{|\Phi^{+}\rangle}=92.0\pm0.6\%$ and $F_{|\Phi^{-}\rangle}=91.1\pm0.7\%$, with an averaged fidelity of 91.5 $\pm0.8\%$. The non-ideality of the fidelity is attributed to the waveguide loss, unbalanced coupling efficiency, imperfect rotation of the polarization elements and misalignment of the polarization analysers.

The chip-to-chip distribution of the four Bell states demonstrates the coherent reversible conversion of our SWAP gate between polarization and spatial-momentum DoF. This demonstration also provides a practical tool for the quantum interconnect of distant photonic platforms with different DoFs towards achieving distributed quantum computation and quantum sensing ^{17,44}.

Discussion

We have successfully demonstrated a deterministic single-photon two-qubit SWAP gate between polarization and spatial-momentum on a silicon chip. The performance of our on-chip SWAP gate can be further improved by optimizing the fabrication parameters and chip coupling. We note that the deviations from unity in the truth-table fidelity mainly arise from the imperfect extinction ratio of the PC-NOT and MC-NOT gates and the MC-NOT gate's unbalanced photon loss. These non-idealities are examined in detail in Supplementary Section X and can be mitigated by more adiabatic polarization-mode conversion and tighter suppression of the cross-polarization. In addition, we note that the waveguide loss and unbalanced coupling efficiency between the $|H\rangle$ and $|V\rangle$ states contribute to a truth-table fidelity reduction by ~0.5%. With recent progress on integrated polarization devices, PBSs with extinction ratios of over 35 dB and polarization rotators with low insertion loss have been realized on a silicon platform³², which can bring our chip's truth-table fidelity up to near-unity. In addition, a silicon-based MZI with an extinction ratio of over 66 dB has been achieved, which will further improve the path-mode projection for quantum state tomography measurements⁴⁵.

The quantum coherence is preserved during the on-chip SWAP process, and the coherent reversible conversion enables quantum interconnectivity between two chips. We note that conversion of photonic quantum states between different DoFs has been demonstrated on chip^{40,46}, but none have demonstrated an on-chip two-qubit SWAP gate operation. With the CMOS-compatible silicon chip-scale platform, high-density photonic integration involving different DoFs might be possible for future applications⁴⁷, extending to high-dimensional quantum gate operation 48,49, with intrinsic good phase stability and compactness. The demonstrated quantum photonic interconnect can facilitate applications exploiting polarization and spatial-momentum entanglement between chip-based subsystems. In addition, the compatibility with microelectronics enables monolithic integration of photon sources, logic circuits and detectors on a silicon platform^{20,50}. Our on-chip SWAP gate paves the way for deterministic chip-scale quantum information processing and provides a photonic quantum interface for interconnected quantum information systems towards achieving a quantum internet.

Online content

Any methods, additional references, Nature Portfolio reporting summaries, source data, extended data, supplementary information, acknowledgements, peer review information; details of author contributions and competing interests; and statements of data and code availability are available at https://doi.org/10.1038/s41566-023-01224-x.

References

- Harrow, A. W. & Montanaro, A. Quantum computational supremacy. Nature 549, 203–209 (2017).
- Preskill, J. Quantum computing in the NISQ era and beyond. Quantum 2, 79 (2018).
- Arute, F. et al. Quantum supremacy using a programmable superconducting processor. *Nature* **574**, 505–510 (2019).
- Zhong, H.-S. et al. Quantum computational advantage using photons. Science 370, 1460–1463 (2020).
- O'Brien, J. L. Optical quantum computing. Science 318, 1567–1570 (2007).

- Knill, E., Laflamme, R. & Milburn, G. J. A scheme for efficient quantum computation with linear optics. *Nature* 409, 46–52 (2001).
- Wang, X.-L. et al. 18-Qubit entanglement with six photons' three degrees of freedom. *Phys. Rev. Lett.* 120, 260502 (2018).
- 8. Kok, P. et al. Linear optical quantum computing with photonic qubits. *Rev. Mod. Phys.* **79**, 135–174 (2007).
- 9. Raussendorf, R. & Briegel, H. J. A one-way quantum computer. *Phys. Rev. Lett.* **86**, 5188–5191 (2001).
- Walther, P. et al. Experimental one-way quantum computing. Nature 434, 169–176 (2005).
- 11. O'Brien, J., Furusawa, A. & Vučković, J. Photonic quantum technologies. *Nat. Photon.* **3**, 687–695 (2009).
- 12. Fiorentino, M. & Wong, F. N. C. Deterministic controlled-NOT gate for single-photon two-qubit quantum logic. *Phys. Rev. Lett.* **93**, 070502 (2004).
- 13. Carolan, J. et al. Universal linear optics. Science **349**, 711–716 (2015).
- Kimble, H. J. The quantum internet. *Nature* 453, 1023–1030 (2008).
- 15. Wehner, S., Elkouss, D. & Hanson, R. Quantum internet: a vision for the road ahead. *Science* **362**, eaam9288 (2018).
- Cacciapuoti, A. S. et al. Quantum internet: networking challenges in distributed quantum computing. *IEEE Netw.* 34, 137–143 (2020).
- Awschalom, D. et al. Development of quantum interconnects for next-generation information technologies. PRX Quantum 2, 017002 (2021).
- Erhard, M., Krenn, M. & Zeilinger, A. Advances in high-dimensional quantum entanglement. *Nat. Rev. Phys.* 2, 365–381 (2020).
- 19. Wang, J., Sciarrino, F., Laing, A. & Thompson, M. G. Integrated photonic quantum technologies. *Nat. Photon.* **14**, 273–284 (2020).
- Wang, J. et al. Multidimensional quantum entanglement with large-scale integrated optics. Science 360, 285–291 (2018).
- Qiang, X. et al. Large-scale silicon quantum photonics implementing arbitrary two-qubit processing. *Nat. Photon.* 12, 534–539 (2018).
- 22. Barz, S. et al. Demonstration of blind quantum computing. *Science* **335**, 303–308 (2012).
- 23. Cirac, J. I., Ekert, A. K., Huelga, S. F. & Macchiavello, C. Distributed quantum computation over noisy channels. *Phys. Rev. A* **59**, 4249–4254 (1999).
- 24. Sheng, Y.-B. & Zhou, L. Distributed secure quantum machine learning. Sci. Bull. **62**, 1025–1029 (2017).
- Fiorentino, M., Kim, T. & Wong, F. N. C. Single-photon two-qubit SWAP gate for entanglement manipulation. *Phys. Rev. A* 72, 012318 (2005).
- Kagalwala, K. H., Di Giuseppe, G., Abouraddy, A. F. & Saleh, B. E. A. Single-photon three-qubit quantum logic using spatial light modulators. *Nat. Commun.* 8, 739 (2017).
- 27. Lu, H.-H. et al. Quantum phase estimation with time-frequency qudits in a single photon. *Adv. Quantum Tech.* **3**, 1900074 (2020).
- 28. Zhang, M. et al. Supercompact photonic quantum logic gate on a silicon chip. *Phys. Rev. Lett.* **126**, 130501 (2021).
- Li, J.-P. et al. Heralded nondestructive quantum entangling gate with single-photon sources. *Phys. Rev. Lett.* 126, 140501 (2021).
- 30. Nielsen, M. A. & Chuang, I. L. Quantum Computation and Quantum Information (Cambridge Univ. Press, 2000).
- 31. Barwicz, T. et al. Polarization-transparent microphotonic devices in the strong confinement limit. *Nat. Photon.* **1**, 57–60 (2007).
- 32. Su, Y., Zhang, Y., Qiu, C., Guo, X. & Sun, L. Silicon photonic platform for passive waveguide devices: materials, fabrication and applications. *Adv. Mater. Technol.* **5**, 1901153 (2020).
- Goi, K. et al. Low-loss partial rib polarization rotator consisting only of silicon core and silica cladding. Opt. Lett. 40, 1410–1413 (2015).

- Horikawa, T. et al. A 300-mm silicon photonics platform for large-scale device integration. *IEEE J. Sel. Top. Quantum Electron*. 24, 8200415 (2018).
- 35. Chang, K.-C. et al. 648 Hilbert space dimensionality in a biphoton frequency comb: entanglement of formation and Schmidt mode decomposition. *NPJ Quantum Inf.* **7**, 48 (2021).
- Xie, Z. et al. Harnessing high-dimensional hyperentanglement through a biphoton frequency comb. Nat. Photon. 9, 536-542 (2015).
- O'Brien, J. L. et al. Quantum process tomography of a controlled-NOT gate. *Phys. Rev. Lett.* 93, 080502 (2004).
- 38. White, A. G. et al. Measuring two-qubit gates. *J. Opt. Soc. Am. B* **24**, 172–183 (2007).
- Hong, C. K., Ou, Z. Y. & Mandel, L. Measurement of subpicosecond time intervals between two photons by interference. *Phys. Rev. Lett.* 59, 2044–2046 (1987).
- Feng, L.-T. et al. On-chip coherent conversion of photonic quantum entanglement between different degrees of freedom. *Nat. Commun.* 7, 11985 (2016).
- 41. Silverstone, J. W. et al. On-chip quantum interference between silicon photon-pair sources. *Nat. Photon.* **8**, 104–108 (2014).
- Llewellyn, D. et al. Chip-to-chip quantum teleportation and multi-photon entanglement in silicon. *Nat. Phys.* 16, 148–153 (2020).
- 43. Kwiat, P. G. et al. New high-intensity source of polarizationentangled photon pairs. *Phys. Rev. Lett.* **75**, 4337–4341 (1995).
- 44. Zhang, Z. & Zhuang, Q. Distributed quantum sensing. *Quantum Sci. Technol.* **6**, 043001 (2021).

- 45. Harris, N. C. et al. Quantum transport simulations in a programmable nanophotonic processor. *Nat. Photon.* **11**, 447–452 (2017).
- 46. Wang, J. et al. Chip-to-chip quantum photonic interconnect by path-polarization interconversion. *Optica* **3**, 407–413 (2016).
- 47. Xiong, C. et al. Compact and reconfigurable silicon nitride time-bin entanglement circuit. *Optica* **2**, 724–727 (2015).
- Gao, X., Erhard, M., Zeilinger, A. & Krenn, M. Computer-inspired concept for high-dimensional multipartite quantum gates. *Phys. Rev. Lett.* 125, 050501 (2020).
- 49. Imany, P. et al. High-dimensional optical quantum logic in large operational spaces. *NPJ Quantum Inf.* **5**, 59 (2019).
- Najafi, F. et al. On-chip detection of non-classical light by scalable integration of single-photon detectors. *Nat. Commun.* 6, 5873 (2015).

Publisher's note Springer Nature remains neutral with regard to jurisdictional claims in published maps and institutional affiliations.

Springer Nature or its licensor (e.g. a society or other partner) holds exclusive rights to this article under a publishing agreement with the author(s) or other rightsholder(s); author self-archiving of the accepted manuscript version of this article is solely governed by the terms of such publishing agreement and applicable law.

© The Author(s), under exclusive licence to Springer Nature Limited 2023

Methods

Chip fabrication

Our on-chip SWAP gate consists of two PC-NOT gates and an MC-NOT gate. The PC-NOT gate is a silicon waveguide device realized by a polarized directional coupler. The silicon MC-NOT gate is realized by a specially designed two-layer polarization rotator that consists of a polarization rotation stage with an asymmetric partial-rib waveguide and a polarization-maintaining mode conversion stage with a nano-tapered waveguide. With further detail provided in Supplementary Section I.B, the MC-NOT consists of three sections, with a middle-section slab height of 110 nm. The core width adiabatically evolves from 300-nm width at the gate input to 180-nm width at the middle-section interface region, and back to 300-nm width at the gate output. With the continuous mode evolution designed into our MC-NOT gate, the insertion losses are ~0.5 dB and 1.0 dB for the TE-to-TM and TM-to-TE polarizations, respectively, while preserving a 20-dB extinction in the TE and TM polarizations. The designed gate is fabricated on a silicon-on-insulator wafer using a CMOS-based process with a KrF excimer laser stepper. The top silicon layer is 220 nm thick and the thickness of the buried oxide layer is $3 \mu m$. The asymmetric partial rib of the core is formed by two-step dry-etching processes, specifically achieved by a developed self-aligned process for this study (detailed in Supplementary Section II). A 2-μm SiO₂ cladding is deposited on top of the core by high-density plasma-enhanced chemical vapour deposition. The total length of the polarization rotator is 360 μm. For photon input-output coupling, our standardized design library with inverse adiabatic couplers is implemented. This consists of a silicon nano-tip of ~180 nm, with mode evolving to the standardized single-mode width. The SiO₂ cladding on the nano-tip forms an oxide waveguide, with air trenches on the lateral transverse sides of the oxide waveguide. Deep reactive ion etching forms the input and output facets. The complete SWAP gate (input-output couplers, PC-NOT and MC-NOT gates) only requires silicon and silicon-oxide interfaces, which are compatible with silicon foundries.

Quantum process tomography

A quantum operation can be completely determined by experimentally measuring the output quantum states from a set of pure input states 30 . Any quantum process can be represented by a χ matrix, which is $2^{2N} \times 2^{2N}$ for an N-qubit operation. Such a χ matrix can be experimentally reconstructed by quantum process tomography 38 . For a fixed set of operators \tilde{E} , the output state after a quantum process for an input state ρ can be expressed in the operator sum representation as $\rho' = \sum_{m,n} \chi \tilde{E}_m \rho E_n^{\dagger}$. For single-qubit process tomography of our on-chip SWAP gate, we selected the operator basis \tilde{E} with four Pauli matrices σ_l , σ_x , σ_y and σ_z . We prepared four linearly independent polarization states $|H\rangle$, $|V\rangle$, $|D\rangle = (|H\rangle + |V\rangle)/\sqrt{2}$ and $|R\rangle = (|H\rangle + i|V\rangle)/\sqrt{2}$ as inputs, and measured houtput states in the spatial-momentum basis $|0\rangle$, $|1\rangle$, $|+\rangle = (|0\rangle + |1\rangle)/\sqrt{2}$ and $|+i\rangle = (|0\rangle + i|1\rangle)/\sqrt{2}$. The process matrix χ of the single-qubit SWAP operation is then expressed as $\chi = \Lambda \begin{pmatrix} \rho_1' & \rho_2' \\ \rho_3' & \rho_4' \end{pmatrix} \Lambda$, where the matrix ρ' is determined via quantum state tomography, and the block matrix Λ is defined as $\Lambda = \frac{1}{2}\begin{pmatrix} I & \sigma_x \\ \sigma_x & -I \end{pmatrix}$.

For two-qubit process tomography of our on-chip SWAP gate, we selected the operator basis $\tilde{E} = \sigma_m \otimes \sigma_n$, where m, n = I, X, Y, Z. We prepared 16 linearly independent states $\rho_{\rm sm,pol} = |i_{\rm sm}j_{\rm pol}\rangle$ as input two-qubit states, where $i_{\rm sm} = 0, 1, +, +i$ and $j_{\rm pol} = H, V, D, R$. The output states were then measured in the same basis with density matrices reconstructed via quantum state tomography. The process matrix χ of the two-qubit SWAP operation can be reconstructed similarly using a block matrix of the measured density matrices by:

$$\chi = K^{\mathsf{T}} \begin{pmatrix} \rho'_{11} & \rho'_{12} & \rho'_{13} & \rho'_{14} \\ \rho'_{21} & \rho'_{22} & \rho'_{23} & \rho'_{24} \\ \rho'_{31} & \rho'_{32} & \rho'_{33} & \rho'_{34} \\ \rho'_{41} & \rho'_{42} & \rho'_{43} & \rho'_{44} \end{pmatrix} K$$

Here, $K = P\Lambda$, $P = I \otimes [M \otimes I]$, $\Lambda = \frac{1}{4}(\sigma_Z \otimes I + \sigma_X \otimes \sigma_X) \otimes (\sigma_Z \otimes I + \sigma_X \otimes \sigma_X)$ and

$$M = \begin{pmatrix} 1 & 0 & 0 & 0 \\ 0 & 0 & 1 & 0 \\ 0 & 1 & 0 & 0 \\ 0 & 0 & 0 & 1 \end{pmatrix}$$

The reconstructed density matrices and process matrices may be nonphysical due to the noise in the measurement process, so we employ the maximum-likelihood estimation for both quantum state and process tomography to find the closest matrix to the measured one³⁸. The process fidelity is defined as $F_{\chi} = \frac{\text{Tr}(\chi\chi_i)}{\text{Tr}(\chi_i)\text{Tr}(\chi_i)}$ for both singe-qubit and two-qubit process tomography, where χ_i is the theoretically ideal process matrix. The purity of the SWAP process (matrix χ) is also evaluated as $P_{\chi} = \frac{\text{Tr}(\chi^2)}{\text{Tr}^2(\chi)}$, which is unity for an ideal process.

Bell-state preparation

The polarization Bell states for the chip-to-chip distribution were prepared by post-selection. We first mixed the signal and idler photons on a 50:50 fibre coupler with orthogonal polarizations. To ensure good temporal overlapping between the signal and idler photons, we swept the relative delay between them to find the HOM dip (as detailed in Supplementary Section VIII) and then rotated the polarization of the signal photons by 90°. The post-selected polarization entanglement was verified after the fibre coupler via polarization projection measurements with 94.2 \pm 0.9% fringe visibility, and $S = 2.664 \pm 0.029$ violating the classical limit by more than 22 s.d. 35,36. The two output ports of the 50:50 fibre coupler were then connected to the top and bottom channels of the first SWAP gate chip. We inserted a pair of a HWP and a QWP at the input of the first SWAP gate chip. The polarization Bell state $|\Psi^{+}\rangle$ can be tuned to $|\Phi^{+}\rangle$ by the HWP or to $|\Psi^{-}\rangle$ by the QWP in one input path. By appropriately orienting the waveplates, we were able to prepare four polarization Bell states for distribution between dual SWAP gate chips⁴³.

Data availability

All the data and methods are presented in the main text and the Supplementary Information. The figures are also available on Figshare at https://doi.org/10.6084/m9.figshare.22590367. The raw datasets generated and/or analysed during the current study are available from the corresponding author upon request. Source data are provided with this paper.

Acknowledgements

We acknowledge discussions with H. Liu, K. Yu, Y. Cho, A. Veitia, T. Zhong and F. Sun and SEM assistance from J. F. McMillan. This work is supported by the National Science Foundation (EFRI-ACQUIRE 1741707, QII-TAQS 1936375, 1919355 and 2008728) and the University of California National Laboratory research programme (LFRP-17-477237).

Author contributions

X.C., K.C.C., Z.X. and Y.S.L. performed the measurements. Y.L., S.K. and X.X. performed the design layout. M.Y., P.G.Q.L. and D.L.K. performed the device nanofabrication. X.C., M.C.S., X.X., A.K.V., J.H.S. and F.N.C.W. contributed to the theory and numerical modelling. X.C., Z.X., X.X., J.H.S., F.N.C.W. and C.W.W. wrote the manuscript, with contributions from all authors.

Competing interests

The authors declare no competing interests.

Additional information

Supplementary information The online version contains supplementary material available at https://doi.org/10.1038/s41566-023-01224-x.

Correspondence and requests for materials should be addressed to Xiang Cheng, Kai-Chi Chang or Chee Wei Wong.

Peer review information *Nature Photonics* thanks Marco Fiorentino and the other, anonymous, reviewer(s) for their contribution to the peer review of this work.

Reprints and permissions information is available at www.nature.com/reprints.